



Ag₃PO₄/reduced graphite oxide sheets nanocomposites with highly enhanced visible light photocatalytic activity and stability

Pengyu Dong, Yuhua Wang*, Baocheng Cao, Shuangyu Xin, Linna Guo, Jia Zhang, Fenghua Li

Department of Materials Science, School of Physical Science and Technology, Lanzhou University, Lanzhou 730000, PR China

ARTICLE INFO

Article history:

Received 7 September 2012
Received in revised form 26 October 2012
Accepted 11 November 2012
Available online 26 November 2012

Keywords:

Reduced graphite oxide sheets
Silver orthophosphate
Nanocomposite
Photocatalysis
Stability

ABSTRACT

A series of Ag₃PO₄ and reduced graphite oxide sheets (RGOs) nanocomposites have been fabricated by a facile chemical precipitation approach in N,N-dimethylformamide (DMF) solvent without any hard/soft templates. The as-prepared Ag₃PO₄/RGOs composites were characterized by X-ray diffraction pattern (XRD), Fourier transform infrared spectra (FTIR), Raman spectroscopy, field emission scanning electron microscopy (SEM), transmission electron microscopy (TEM), and ultraviolet-visible (UV-vis) diffuse reflectance spectroscopy (DRS). It is found that the nano-sized Ag₃PO₄ particles are deposited on the surfaces of RGOs. The Ag₃PO₄/RGOs nanocomposites exhibit enhanced photocatalytic activity for the photodegradation of organic methyl orange (MO) and methylene blue (MB) under visible light irradiation. The photocatalytic rate of Ag₃PO₄/2.1 wt% RGOs nanocomposite is 3 and 2 times of that of pure Ag₃PO₄ nanoparticles for the degradation of MO and MB, respectively. Furthermore, the photocatalytic and structural stability of Ag₃PO₄ is greatly enhanced. It is suggested that RGOs can be used as protective coatings that partially inhibit the photocorrosion of Ag₃PO₄. Overall, this work could provide a new approach to the improvement not only in the photocatalytic activity but also the stability of photocorrosion catalysts.

© 2012 Elsevier B.V. All rights reserved.

1. Introduction

It is well known that environmental pollution is affecting human survival and development. Photocatalytic technology is considered as an efficient, stable, and environmentally friendly method in the field of environmental pollution control [1]. During the past 20 years, TiO₂ has been widely used as a photocatalyst in the photodegradation of organic pollutants due to its chemical stability, nontoxicity, favorable optoelectronic properties, and low cost. However, TiO₂ cannot make use of visible light that accounts for 45% of solar spectrum because of a large band gap (3.2 eV). Moreover, the low separation rate of the photoexcited electron–hole in TiO₂ leads to the limited quantum efficiency [2]. Therefore, the discovery of new active and efficient visible-light-driven photocatalysts attracts much attention.

More recently, a breakthrough on visible-light-driven photocatalysts was made by Ye et al., who reported the use of Ag₃PO₄ as an active visible-light-driven photocatalyst for the oxidation of water and photodecomposition of organic compounds [3–5]. These works demonstrated that Ag₃PO₄ photocatalyst can achieve high quantum efficiency under visible light irradiation. However, it should

be noted that there are still some limitations in the Ag₃PO₄ photocatalytic system. First of all, the particle size of Ag₃PO₄ is relatively large (0.5–2 μm) which actually limits the photocatalytic performance. To enhance photocatalytic activity of this new material, it is desirable to synthesize nano-sized Ag₃PO₄ particles for nano-sized particles have higher surface area which is beneficial to the photocatalytic reaction [6]. In addition to the problem of particle size, the Ag₃PO₄ photocatalyst suffers from serious stability issue which is the main hindrance for the practical application of Ag₃PO₄ as a recyclable and highly efficient photocatalyst. It is well known that Ag₃PO₄ is slightly soluble in aqueous solution, which reduces its structural stability. Moreover, the conduction band potential of Ag₃PO₄ is more positive than that of the hydrogen potential [7]. Thus, Ag₃PO₄ absorbs a photon to generate an electron and a hole, and then the electron combines with an interstitial silver ion (Ag⁺) to give a silver atom (Ag), which results in the photocorrosion of Ag₃PO₄ in the absence of a sacrificial reagent. The appeared black metallic Ag particles would suspend in the photocatalytic reaction systems and attach onto the surface of the Ag₃PO₄ catalyst, which would inevitably prevent the visible light absorption and decrease the photocatalytic activity [8]. Therefore, it is a highly crucial task to improve the photocatalytic stability of Ag₃PO₄ while maintains its high photocatalytic activity [2]. Recent report indicated that the insoluble AgX (X=Cl, Br, I) nanoshells on the surface of Ag₃PO₄ could improve its photocatalytic activity and stability [8]. In addition, various coupled systems such as Ag₃PO₄/TiO₂

* Corresponding author. Tel.: +86 931 8912772; fax: +86 931 8913554; mobile: +86 13919816967.

E-mail address: wyh@lzu.edu.cn (Y. Wang).

[9,10], $\text{Ag}_3\text{PO}_4/\text{Ag}$ [2,11], $\text{Ag}_3\text{PO}_4/\text{SnO}_2$ [12], $\text{Fe}_3\text{O}_4/\text{Ag}_3\text{PO}_4$ [13], and carbon quantum dots/ Ag_3PO_4 [14] composites have recently been developed to improve the photocatalytic activity and stability of Ag_3PO_4 .

Reduced graphite oxide (RGO) or graphene nanosheets, single layers of carbon atoms tightly packed into 2-dimensional (2D) honeycomb sp^2 carbon lattices, have received much attention in the past few years [15,16]. Apart from its unique electronic properties [17], RGO has several other excellent attributes, such as the large theoretical specific surface area [18] and good chemical stability [19]. Moreover, the large specific surface areas of RGO sheets (RGOs) facilitate attachment of inorganic nanomaterials [20,21]. Thus, the combination of photocatalyst and RGOs is promising to possess excellent adsorptivity, conductivity, and controllability simultaneously, which could facilitate effective photodegradation of pollutants [22]. Considering these remarkable properties of RGOs and the limitations of the Ag_3PO_4 photocatalytic system, the combination of RGOs and Ag_3PO_4 could be regarded as an ideal strategy to construct stable and efficient composite photocatalyst.

In this work, $\text{Ag}_3\text{PO}_4/\text{RGOs}$ nanocomposites were prepared by a chemical precipitation method for the first time for the purpose of improving the visible light photocatalytic activity and stability of Ag_3PO_4 . The synthesis method is less finicky, low-cost, and effective for large-scale production. Moreover, we firstly demonstrate that nano-sized Ag_3PO_4 could be synthesized in the organic solvent (DMF). In addition, it is found that the content of RGOs obviously affects the photocatalytic activity of $\text{Ag}_3\text{PO}_4/\text{RGOs}$ nanocomposites. More importantly, the addition of RGOs could enhance the structural and photocatalytic stability of Ag_3PO_4 .

2. Experimental

2.1. Sample preparation

RGO was synthesized by a reported method [23]. Details are presented in [Supplementary data](#).

In a typical synthesis of $\text{Ag}_3\text{PO}_4/\text{RGOs}$ nanocomposite, at first, a certain amount of the RGO was dispersed into 10 mL of N,N-dimethylformamide (DMF) with sonicating for 2 h to form the dispersion of RGOs. Then, 1 mmol of AgNO_3 was added into the dispersion of RGOs under vigorous stirring. After stirring for 10 min, H_3PO_4 (1 mL, 85%) dissolved in 5 mL of ethanol was then added dropwise into the above dispersion under stirring. The mixture was stirred for a fixed time. The obtained precipitates were separated by centrifuge followed by washing with ethanol and deionized water for several times, respectively. The product was then dried in a vacuum oven at 60 °C. The contents of adding RGOs are 1, 2, 3, 4 and 5 mg, and the obtained samples are labeled as $\text{Ag}_3\text{PO}_4/0.7\text{ wt\% RGOs}$, $\text{Ag}_3\text{PO}_4/1.4\text{ wt\% RGOs}$, $\text{Ag}_3\text{PO}_4/2.1\text{ wt\% RGOs}$, $\text{Ag}_3\text{PO}_4/2.8\text{ wt\% RGOs}$, and $\text{Ag}_3\text{PO}_4/3.5\text{ wt\% RGOs}$, respectively. For comparison purpose, pure Ag_3PO_4 nanoparticles were synthesized without the addition of RGOs. Micron-sized Ag_3PO_4 and N-doped TiO_2 were synthesized by previously reported methods [3,24], respectively.

2.2. Characterization

X-ray diffraction (XRD) experiments were carried out with a D/max-2400 diffractometer (Rigaku, Japan) using Cu-K α radiation. Fourier transform infrared spectra (FTIR) of the samples were recorded between 400 and 4000 cm^{-1} on a Nicolet NEXUS 670 FTIR spectrometer. A Renishaw inVia Raman microscope with 532 nm laser excitation was used to record the Raman spectrum of the samples. The morphologies of the samples were examined by scanning electron microscopy (SEM, Hitachi S-4800). A

FEI Tecnai G2 F30 transmission electron microscope, equipped with a Gatan imaging filter (GIF) system, was used for transmission electron microscopy (TEM), high-resolution transmission electron microscopy (HRTEM), selected-area electron diffraction pattern (SAED), and energy dispersive X-ray spectra (EDX) work. Ultraviolet-visible diffuse reflectance (UV-vis DRS) absorption spectra were measured using a Perkin Elmer 950 spectrometer, while BaSO_4 was used as a reference. Total organic carbon (TOC) of the dye solutions was analyzed using the Elementar TOC analyzer.

2.3. Evaluation of photocatalytic activity

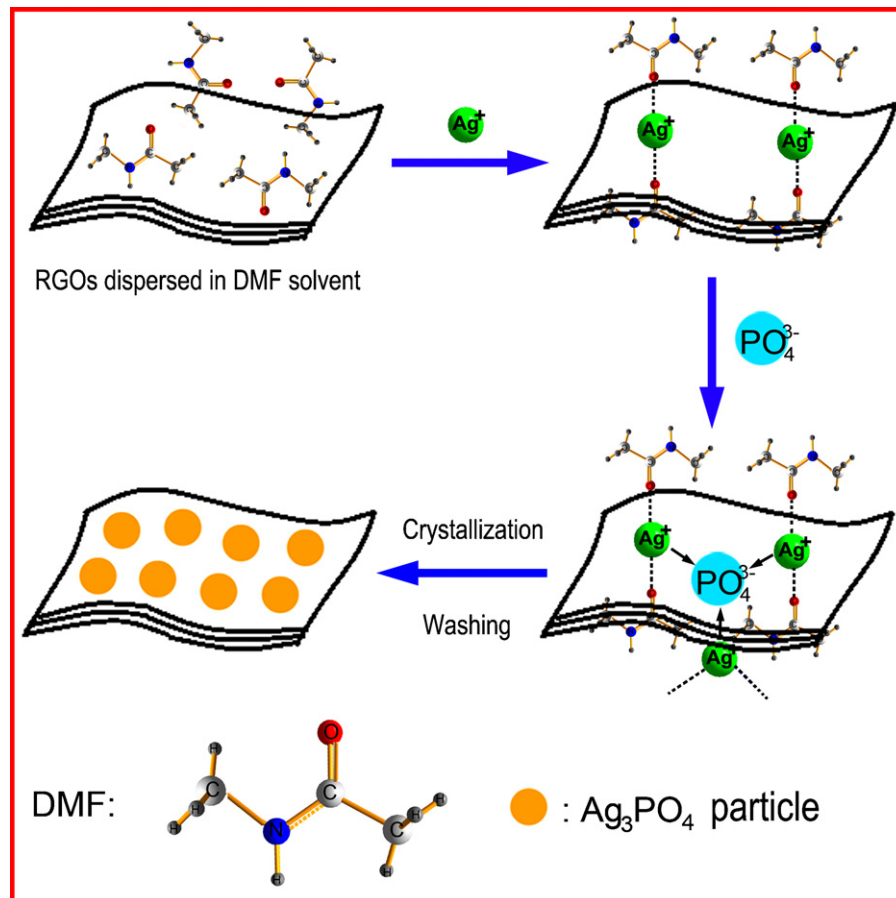
The photocatalytic activity of catalysts was measured by the decomposition of methyl orange (MO, pH 7) and methylene blue (MB) in a reactor at room temperature. In a typical process for degradation of a dye, 20 mg of photocatalyst was suspended in the dye solution (10 mg/L, 70 mL). Before irradiation, the suspensions were stirred in the dark for 60 min to ensure the establishment of adsorption–desorption equilibrium. A 350 W Xe lamp with a cutoff filter of 420 nm was employed for the visible-light irradiation source and positioned 20 cm away from the reactor to trigger the photocatalytic reaction. A certain volume of suspension were withdrawn at selected times for analysis. After recovering the photocatalyst by centrifugation, the concentration of dye solution was analyzed by measuring the light absorption of the clear solution at 465 nm (λ_{max} for MO solution) or 664 nm (λ_{max} for MB solution) using a spectrophotometer (WFJ-7200, Unico, USA). The percentage of degradation was calculated by C/C_0 . Here, C is the concentration of remaining dye solution at each irradiated time interval, while C_0 is the initial concentration.

To test the stability and reusability of $\text{Ag}_3\text{PO}_4/\text{RGOs}$ nanocomposite, the cycling runs in photocatalytic degradation of MB in the presence of $\text{Ag}_3\text{PO}_4/2.1\text{ wt\% RGOs}$ were checked. After one cycle, the photocatalyst was filtrated and washed thoroughly with deionized water, and then fresh MB solution (10 mg/L) was added to the photocatalyst to begin the next cycling run. Three consecutive cycles were completed and each cycle lasted for 120 min.

3. Results and discussion

RGOs are hydrophobic and readily agglomerate in hydrophilic solvents [25]. The good dispersity of RGOs into solvents can prevent agglomeration, which is very important to prepare homogeneous graphene-based composites [26–28]. It was reported that homogeneous colloidal suspension of RGOs could be produced in DMF [28,29]. Hence, we dispersed the as-synthesized RGOs into DMF with sonication and prepared the Ag_3PO_4 nanoparticles in DMF solvent. Besides that, RGOs have large specific surface area, which facilitates the deposition of nanoparticles. The process for preparing $\text{Ag}_3\text{PO}_4/\text{RGOs}$ nanocomposite is illustrated in [Scheme 1](#). It starts with the dispersion of RGOs in DMF solvent, which means that the DMF molecules could absorb on the surfaces of RGOs. In addition, it is worth noting that the silver ions (Ag^+) and amide (e.g. DMF) could form the weekly bound $[\text{Ag}(\text{amide})]^+$ complex [30], and thus the Ag^+ ions could be located on the surfaces of RGOs. When PO_4^{3-} ions were added into the dispersion, strong chemical combination occurred between the Ag^+ ions in the $[\text{Ag}(\text{amide})]^+$ complex and PO_4^{3-} ions, which leads to the crystallization of Ag_3PO_4 nanoparticles on the surfaces of RGOs. Finally, the desired $\text{Ag}_3\text{PO}_4/\text{RGOs}$ nanocomposite was obtained after washing with ethanol and deionized water for several times, respectively.

Crystallinity is regarded as one of important factors in determining photocatalytic activity [31]. The reaction time affects the crystallinity of $\text{Ag}_3\text{PO}_4/\text{RGOs}$ composite, as shown in [Fig. S1 \(in Supplementary data\)](#). When the reaction time prolongs to 6 h, the



Scheme 1. Synthetic procedure for the Ag_3PO_4 /RGOs nanocomposite.

Ag_3PO_4 /RGOs composite shows remarkably improved intensities of XRD peaks, suggesting the improved crystallinity. The well-crystallized phase could facilitate the transfer of the photoinduced electrons, which decreases the probability of recombination with photoinduced holes and thus enhances the quantum efficiency of photocatalysis [32]. Therefore, the pure Ag_3PO_4 and a series of Ag_3PO_4 /RGOs composites were synthesized under the optimized conditions (with reaction time of 6 h).

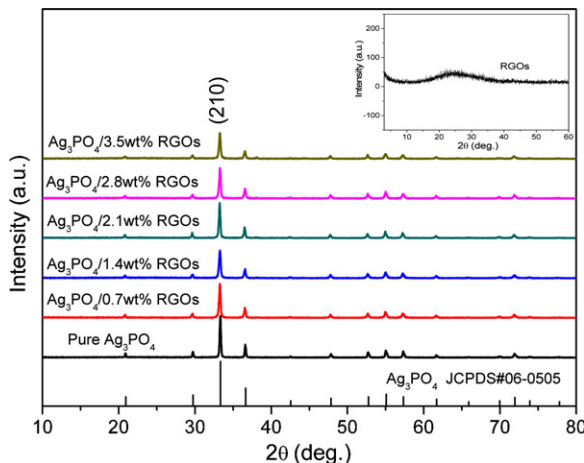


Fig. 1. XRD patterns of as-prepared Ag_3PO_4 and Ag_3PO_4 /RGOs composites with various RGOs contents. The inset is the XRD pattern of the obtained RGOs.

Fig. 1 shows the XRD patterns of as-prepared Ag_3PO_4 and Ag_3PO_4 /RGOs composites. All the diffraction peaks of as-prepared Ag_3PO_4 could be indexed to the cubic Ag_3PO_4 phase, demonstrating that pure Ag_3PO_4 could be synthesized in DMF solvent. The XRD patterns of Ag_3PO_4 /RGOs composites show the phase of Ag_3PO_4 . No diffraction peaks of RGOs can be observed in these composites, indicating the absence of layer-stacking regularity of RGOs or the relatively low content of RGOs in the composite [33]. The inset of **Fig. 1** shows the XRD pattern of the obtained RGOs, which reveals a very broad diffraction peak. The broad nature of reflection peak of RGOs may indicate multilayer without uniform interlayer spacing.

Fig. 2 shows the FTIR spectra of GO, RGOs, pure Ag_3PO_4 , and Ag_3PO_4 /RGOs composite. The FTIR spectrum of GO shows a strong absorption band at 3428 cm^{-1} due to the O–H stretching vibration. It also exhibits bands around 1727 cm^{-1} due to the C=O stretching of COOH groups situated at edges of GO sheets and 1622 cm^{-1} due to the O–H bending vibration [34]. After the reduction process, the intensities of the absorption bands due to the O–H stretching vibration (3428 cm^{-1}) and C=O stretching vibration (1727 cm^{-1}) decrease significantly, and the band at 1622 cm^{-1} is absent. Instead, a new absorption band appears at 1567 cm^{-1} , which is attributed to the skeletal vibration of the graphene sheets [35]. Thus, the FTIR spectra of GO and RGOs demonstrate that GO was reduced effectively when using NaBH_4 as the reducing agent. In pure Ag_3PO_4 and Ag_3PO_4 /RGOs composite, a strong and broad absorption around 3100 cm^{-1} and a sharp band at 1655 cm^{-1} were observed, which could be attributed to the stretching vibration of O–H and the bending vibration of H–O–H of water molecules, respectively. Two absorption bands are also observed in the spectra of pure Ag_3PO_4

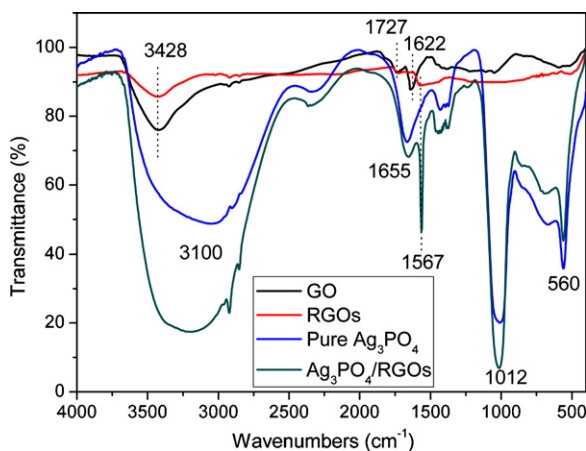


Fig. 2. FTIR spectra of GO, RGOs, pure Ag_3PO_4 and Ag_3PO_4 /2.1 wt% RGOs composite.

and Ag_3PO_4 /RGOs composite at 1012 and 560 cm^{-1} . These two bands can be assigned to molecular vibrations of the phosphate (PO_4^{3-}) [36,37]. A further observation indicates that Ag_3PO_4 /RGOs composite shows an intense sharp band at 1567 cm^{-1} due to the skeletal vibration of the graphene sheets in comparison to that of pure Ag_3PO_4 , proving the existence of RGOs in the Ag_3PO_4 /RGOs composite.

Raman spectroscopy is a powerful non-destructive tool to characterize the crystalline quality of carbon and can be used to prove the existence of RGOs in the Ag_3PO_4 /RGOs composite. As shown in Fig. 3, the G-band around 1590 cm^{-1} and D-band around 1330 cm^{-1} are observed in the Raman spectrum of RGOs, corresponding to the E_{2g} phonon of sp^2 -bonded carbon atoms in a two-dimensional hexagonal lattice, as well as the defects and disorder carbon in the graphite layers, respectively [38]. The pure Ag_3PO_4 shows two bands: an intense sharp band at 922 cm^{-1} and a weak broader band at 1012 cm^{-1} . These bands are attributed to the $(\text{PO}_4)^{3-}$ symmetric and antisymmetric stretching vibrations [39,40]. Besides the bands attributed to the PO_4^{3-} vibrations, two characteristic peaks at about 1330 cm^{-1} (D band) and 1590 cm^{-1} (G band) for the graphitized structures are observed in the Raman spectrum of Ag_3PO_4 /RGOs composite, suggesting the existence of RGOs in the Ag_3PO_4 /RGOs composite. This result suggests the integration of Ag_3PO_4 and RGOs, which is consistent with the FTIR results.

It is observed that the distribution of Ag_3PO_4 nanoparticles on the surfaces of RGOs is non-uniform: Ag_3PO_4 nanoparticles gathered in some areas while dispersed in other areas. A gathered area

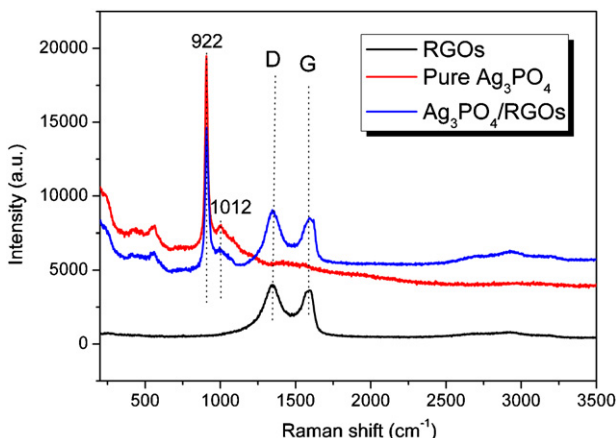


Fig. 3. Raman spectra of RGOs, pure Ag_3PO_4 and Ag_3PO_4 /2.1 wt% RGOs composite.

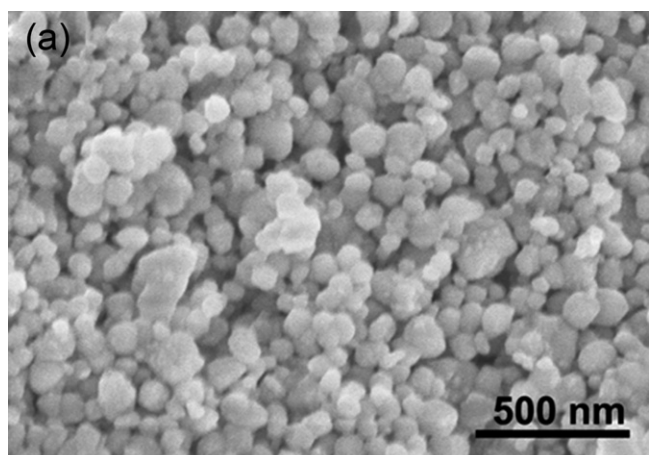


Fig. 4. SEM image (a) and the corresponding particle size distribution (b) for Ag_3PO_4 /2.1 wt% RGOs composite.

was selected, as shown in Fig. 4a, in which we could obtain enough particles (about 240 particles) to make the statistical average particle size more accurately. Fig. 4b shows the average particle size taken from statistics analysis by measuring cross diagonals of these Ag_3PO_4 particles, which is about 79 nm. It is clear that the particle size of as-prepared nano-sized Ag_3PO_4 particles is much smaller than that of the micron-sized Ag_3PO_4 as previously reported [3]. It is also noticed that most of the Ag_3PO_4 particles have a spherical shape.

Fig. 5 displays the TEM images of pure Ag_3PO_4 and Ag_3PO_4 /RGOs nanocomposite. The particle size of as-prepared pure Ag_3PO_4 is in the range of 60–100 nm (Fig. 5a). The TEM image of as-prepared RGOs is shown in Fig. S2. It is observed that the as-prepared RGOs have a crumpled layered structure. To confirm the formation of Ag_3PO_4 /RGOs nanocomposite structure, TEM images were recorded and shown in Fig. 5b–c. It can be seen that spherical Ag_3PO_4 nanoparticles are dispersed on the surfaces of RGOs in the Ag_3PO_4 /RGOs composite, and the particle size of Ag_3PO_4 nanoparticles is in the range of 50–90 nm, which is in agreement with the mean crystal size value of 79 nm as mentioned above. The TEM images of Ag_3PO_4 /RGOs nanocomposites with other RGOs contents are shown in Fig. S3, which also indicates that the Ag_3PO_4 nanoparticles are adequately distributed on the surfaces of RGOs. HRTEM image (Fig. 5d) indicates that the Ag_3PO_4 nanoparticle on the surface of RGO sheet is well crystallized. The angle between the crossing fringes is 66°, and the measured values of fringes are 0.239 and 0.264 nm, corresponding to the crystalline planes of cubic phase of Ag_3PO_4 (2 1 1) and (2 1 0). The SAED pattern

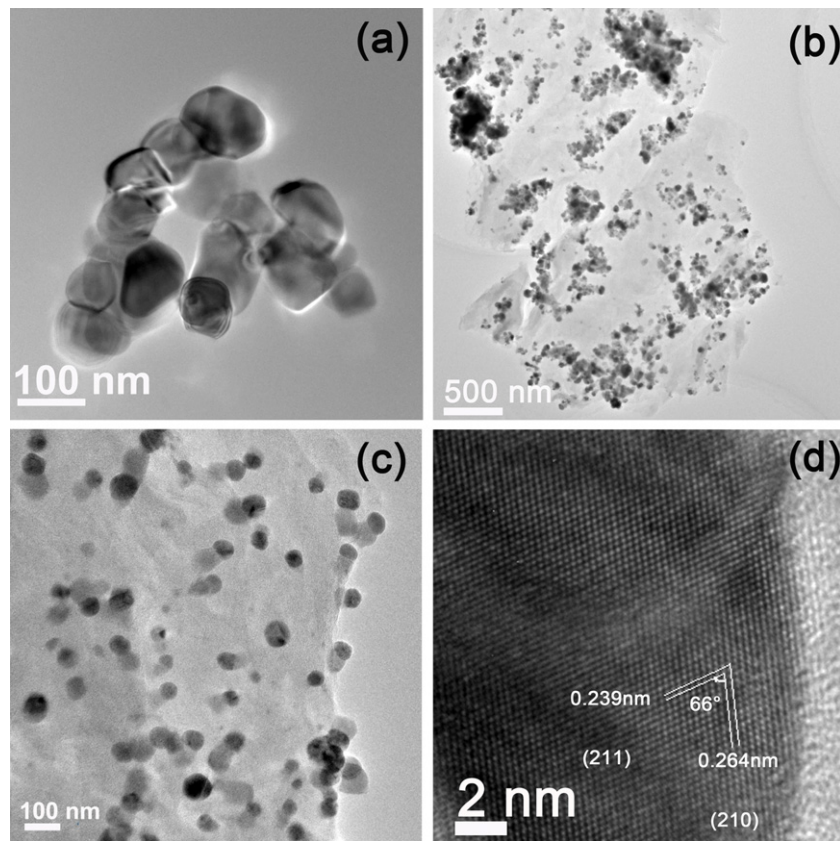


Fig. 5. (a) TEM image of pure Ag_3PO_4 nanoparticles, (b)–(c) TEM images of Ag_3PO_4 /2.1 wt% RGOs nanocomposite, and (d) HRTEM image of a single Ag_3PO_4 nanoparticle in the Ag_3PO_4 /2.1 wt% RGOs nanocomposite.

of Ag_3PO_4 /RGOs nanocomposite (Fig. S4) displays the diffraction spots of Ag_3PO_4 , revealing the monocrystal nature of each Ag_3PO_4 nanoparticle. The EDX patterns of pure Ag_3PO_4 and Ag_3PO_4 /RGOs nanocomposite are shown in Fig. S5. It can be seen that, except for the Ag, P and O peaks coming from Ag_3PO_4 , the intensity of C peak corresponding to RGOs is enhanced significantly in Ag_3PO_4 /RGOs nanocomposite. This result also confirms the existence of RGOs in Ag_3PO_4 /RGOs nanocomposite.

The light-absorbance property of pure Ag_3PO_4 , and Ag_3PO_4 /RGOs nanocomposites was probed with UV-vis absorption spectra, as shown in Fig. 6. Pure Ag_3PO_4 shows a sharp fundamental absorption edge at about 520 nm. The absorption edges of Ag_3PO_4 can also be detected at around 520 nm in the spectra of Ag_3PO_4 /RGOs nanocomposites. It should be noted

that the absorption edges are not shifted for all Ag_3PO_4 /RGOs nanocomposites, indicating the RGOs in the composites are free carbon instead of the incorporated carbon [41]. Hence, an intense and broad background absorption in the visible light region (above 520 nm) instead of a band gap energy decrease is observed. Moreover, with the increase of RGOs content in composite samples, the absorption intensity in the visible light region (above 520 nm) becomes more pronounced, which is in agreement with the color of Ag_3PO_4 /RGOs nanocomposites. It is observed that the color of the composite samples becomes darker (from pale yellow to dark yellow) when an amount of black RGOs are introduced into the pure Ag_3PO_4 nanoparticles. Similar phenomena have been observed in the case of TiO_2 /RGOs composite [42,43].

Before visible light irradiation, the sample suspension was stirred for 60 min in the dark to reach the adsorption–desorption equilibrium. The adsorption–desorption equilibriums of MO and MB are shown in the Light-off periods of Fig. 7a–b. It is found that most of the adsorption of dyes occurs within 30 min, and the Ag_3PO_4 /RGOs nanocomposites exhibit higher adsorption property than P25 as well as pure Ag_3PO_4 , which could be due to the high surface area of RGOs in the composite that increases the adsorption of dye molecules. The higher adsorption of dyes could lead to the easier and faster photocatalytic degradation process, because photocatalytic reactions are typically surface-based processes and the photocatalytic efficiency is closely related to the adsorption property of dyes on the surfaces of photocatalysts [44]. In contrast, the desorption of dyes can be ignored. Moreover, it could be noted that MB molecules are easier to be adsorbed than MO molecules. For example, the MB molecules remained at 78% while MO molecules 90% in the solution after adsorption–desorption equilibrium in the dark when using Ag_3PO_4 /3.5 wt% RGOs nanocomposite as the photocatalyst.

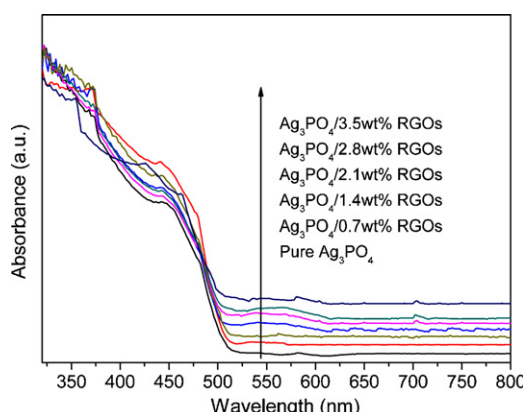


Fig. 6. UV-vis absorption spectra of pure Ag_3PO_4 , and Ag_3PO_4 /RGOs nanocomposites with various RGOs contents.

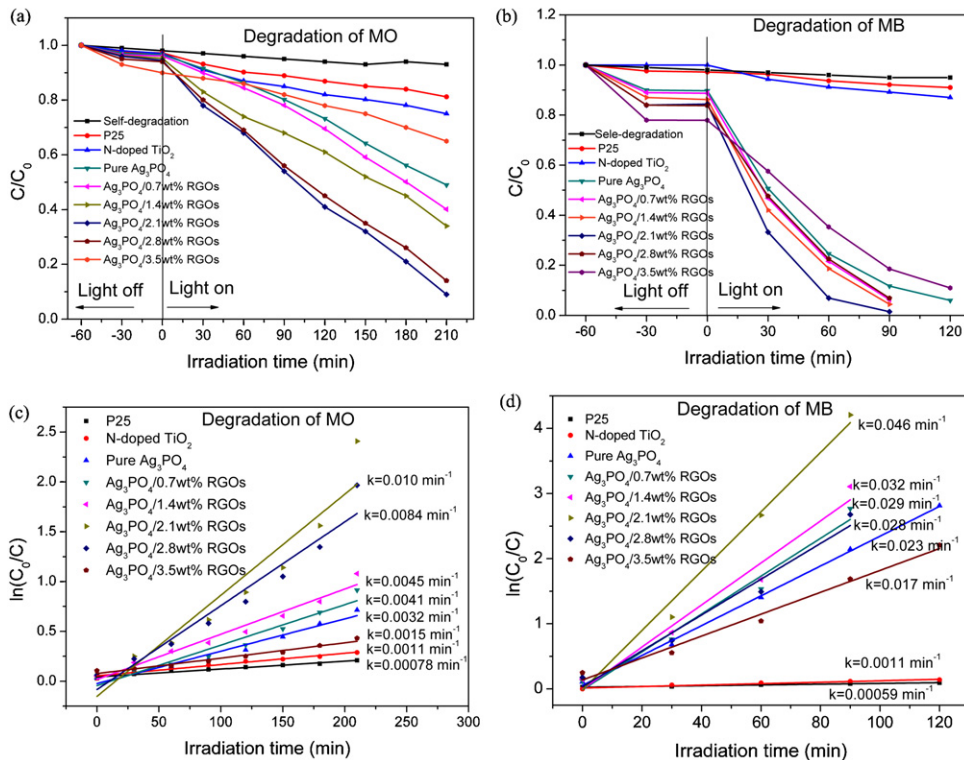


Fig. 7. Variation of MO (a) and MB (b) concentration against irradiation time using P25, N-doped TiO₂, pure Ag₃PO₄, Ag₃PO₄/RGOs nanocomposites with various RGOs contents, and without photocatalyst in the dark and under visible light irradiation; plots of ln(C₀/C) versus irradiation time for MO (c) and MB (d) representing the fit using a pseudo-first-order reaction rate.

The photocatalytic activity of samples was then investigated. It should be pointed out that the self-degradation of MO and MB was not obvious, indicating the stabilization of MO and MB. It can be seen that pure Ag₃PO₄ and Ag₃PO₄/RGOs nanocomposites exhibit higher photocatalytic activity than N-doped TiO₂ and bare P25 powders during the decomposition of MO and MB. It should also be mentioned that pure Ag₃PO₄ nanocrystals show higher photocatalytic activity than micron-sized Ag₃PO₄ (Fig. S6). The photocatalytic degradation efficiency of MO for pure Ag₃PO₄ and Ag₃PO₄/RGOs nanocomposites follows the order Ag₃PO₄/2.1 wt% RGOs > Ag₃PO₄/2.8 wt% RGOs > Ag₃PO₄/1.4 wt% RGOs > Ag₃PO₄/0.7 wt% RGOs > pure Ag₃PO₄ > Ag₃PO₄/3.5 wt% RGOs, as shown in the Light-on period of Fig. 7a. Clearly, the photocatalytic activity of Ag₃PO₄/0.7 wt% RGOs nanocomposite is only slightly higher than that of pure Ag₃PO₄. Further increasing the RGOs content in the composite could lead to a significant increase of photocatalytic activity compared to pure Ag₃PO₄. About 51% and 92% of the initial MO molecules were decomposed by pure Ag₃PO₄ and Ag₃PO₄/2.1 wt% RGOs nanocomposite after 210 min, respectively. For the degradation of MB (in the Light-on period of Fig. 7b), Ag₃PO₄/2.1 wt% RGOs nanocomposite also shows the best photocatalytic degradation ability among these Ag₃PO₄/RGOs nanocomposites with various RGOs contents. As mentioned above, MO and MB molecules could be effectively adsorbed on the surfaces of Ag₃PO₄/RGOs composite, which provide the possibility of occurrence of dye-sensitized photocatalytic decomposition under visible light irradiation. The conduction and valence band potentials of Ag₃PO₄ are +0.45, +2.9 V versus a normal hydrogen electrode (NHE), respectively [3]. Thus, the work function (E) of conduction and valence band potentials of Ag₃PO₄ versus a vacuum, can be calculated to be about -4.95 and -7.40 eV, respectively, according to the equation [45–47]:

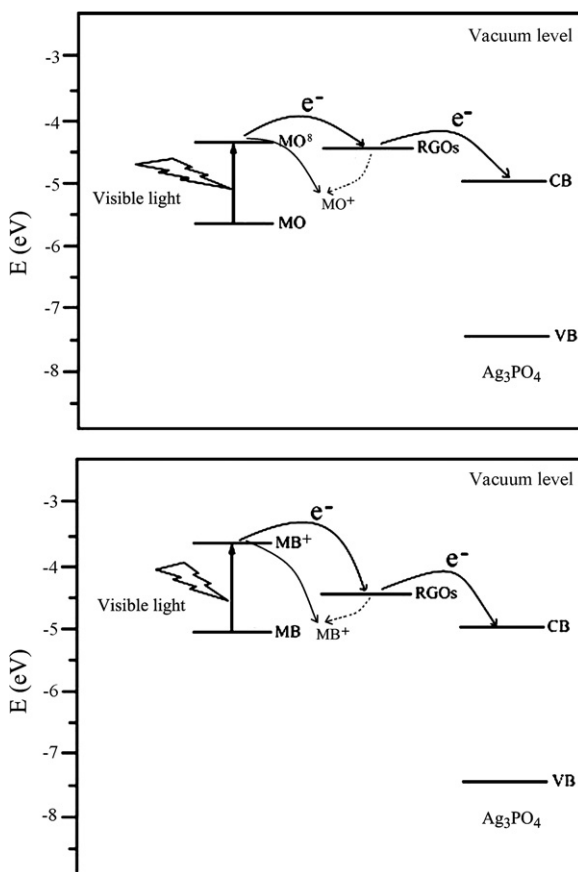
$$E(\text{eV}) = -4.5 - E_{\text{NHE}}(\text{V}) \quad (1)$$

According to the literature [23,48,49], the calculated work functions of RGOs and the excited MB (MB*) are -4.39, and -3.60 eV, respectively. The reduction potential of MO (MO*) versus a saturated calomel electrode (SCE) can be calculated by the equation [50,51]:

$$E_{\text{SCE}}(\text{V}) = -0.058 \text{ pH} \quad (2)$$

Here pH is 7 in this work. Thus, the calculated E_{SCE} of MO* should be about -0.41 V corresponding to -0.17 V versus NHE and -4.33 eV versus a vacuum. Considering the work functions of MO* (-4.33 eV), MB* (-3.60 eV), RGOs (-4.39 eV), and the conduction band potential of Ag₃PO₄ (-4.95 eV), direct electron transfer from MO* or MB* to RGOs is thermodynamically favorable, and the injected electron can further move to the conduction band of Ag₃PO₄ since the energy level of RGOs is higher than that of the conduction band of Ag₃PO₄, as displayed in Scheme 2. Here, the RGOs act as an electron mediator [52], facilitating the electron transfer from MO* or MB* to Ag₃PO₄. The efficient electron transfer process hinders the recombination between the excited electrons and the produced MO⁺ or MB⁺ radicals [53] (dotted lines in Scheme 2), which is responsible for the enhanced photocatalytic performance of Ag₃PO₄/RGOs composite under visible light irradiation [54,55]. However, the photocatalytic activity decreases when the RGOs content in the Ag₃PO₄/RGOs nanocomposite exceeds 2.1 wt%, even though the Ag₃PO₄/2.8 wt% RGOs and Ag₃PO₄/3.5 wt% RGOs composites show stronger visible light absorption and higher adsorption capacity of dyes. This is because that the introduction of a large percentage of black RGOs could lead to a shield of the active sites on the photocatalyst surface [56,57].

Furthermore, the Ag₃PO₄/2.1 wt% RGOs nanocomposite required 60 min to degrade 92% of the MB solution while 210 min needed for degradation of MO. This result clearly demonstrates that Ag₃PO₄/RGOs nanocomposites show much faster photodegradation rate on MB than MO. In general, the photocatalytic selectivity



Scheme 2. The electron transfer diagrams of MO (a) or MB (b), RGOs, and Ag_3PO_4 during the photocatalytic degradation process under visible light irradiation.

of catalyst is related to the selective adsorption of dyes on the surface of catalyst. As mentioned above, the adsorption–desorption equilibrium curves demonstrate that positively charged MB molecules are easier to be adsorbed than negatively charged MO molecules, which could be associated with the RGOs in the composite. This is because RGOs could gather many negative charges resulting from the transportation of photogenerated electrons by RGOs, and thus the positively charged MB molecules would preferentially adsorb on the surfaces of RGOs and then the MB molecules would preferentially degrade [58,59]. On the contrary, the MO molecules exist in its negatively charged form when dissolve in water [60–62], and hence the RGOs in the composite experience electrostatic repulsion, resulting in lower adsorption and degradation rate.

The kinetics of these photocatalytic reactions can be described using a first order reaction for low concentrations of MB and MO solutions, as displayed in Fig. 7c–d. The apparent rate constants (k , min^{-1}), determined from the slopes of $\ln(C_0/C)$ versus irradiation time, are 0.0032 min^{-1} for pure Ag_3PO_4 and 0.01 min^{-1} for $\text{Ag}_3\text{PO}_4/2.1 \text{ wt\% RGOs}$ nanocomposite during the decomposition of MO. In comparison, the apparent rate constants are 0.028 min^{-1} for pure Ag_3PO_4 and 0.046 min^{-1} for $\text{Ag}_3\text{PO}_4/2.1 \text{ wt\% RGOs}$ nanocomposite during the decomposition of MB. Remarkably, the photocatalytic rate of $\text{Ag}_3\text{PO}_4/2.1 \text{ wt\% RGOs}$ nanocomposite is 3 and 2 times of that of pure Ag_3PO_4 for degradation of MO and MB, respectively.

TOC during the photocatalytic reactions was monitored to investigate the mineralization of MO and MB. The experimental results are shown in Fig. 8. After 210 min photodegradation, the TOC removal percentages of MO in the presence of pure Ag_3PO_4 and $\text{Ag}_3\text{PO}_4/2.1 \text{ wt\% RGOs}$ composite were 39% and 77%,

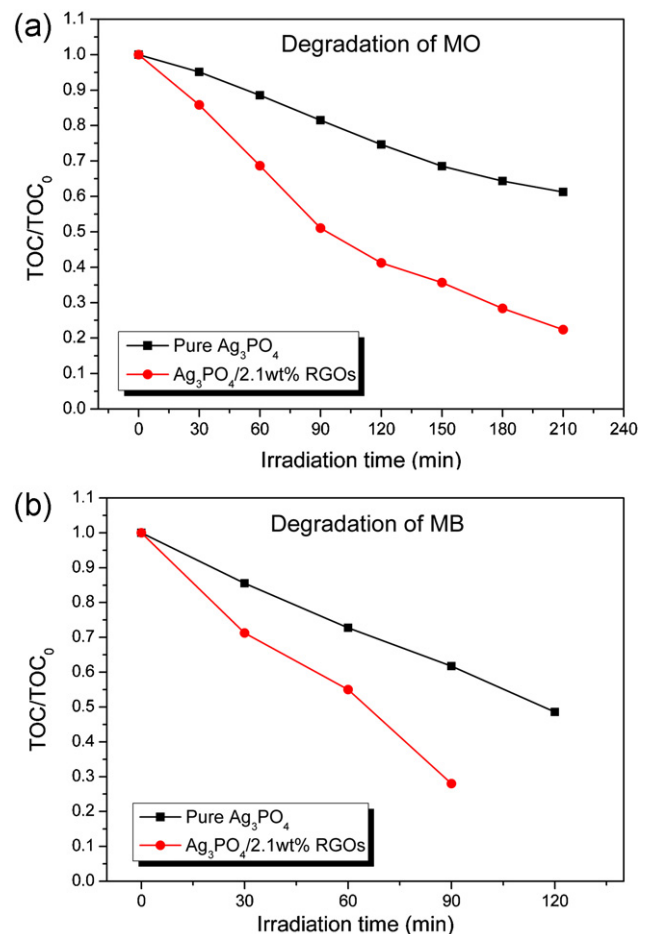


Fig. 8. TOC removal of MO (a) and MB (b) in the presence of pure Ag_3PO_4 and $\text{Ag}_3\text{PO}_4/2.1 \text{ wt\% RGOs}$ composite.

respectively. The TOC removal percentage of MB for pure Ag_3PO_4 sample after 120 min irradiation was found to be 51%, while 72% for $\text{Ag}_3\text{PO}_4/2.1 \text{ wt\% RGOs}$ composite after 90 min irradiation. These results clearly demonstrate that the MO and MB are significantly decomposed, and the TOC removal percentage for pure Ag_3PO_4 is less than that for $\text{Ag}_3\text{PO}_4/2.1 \text{ wt\% RGOs}$ composite, which is consistent with the photocatalytic degradation results (Fig. 7). Additionally, it is noticed that the TOC removal percentage is lower than the discoloration percentage of dyes, indicating the dye molecules are destroyed, but not completely mineralized to inorganic molecules [11].

Overall, the above results clearly indicate that the $\text{Ag}_3\text{PO}_4/\text{RGOs}$ nanocomposites with proper amounts of RGOs synthesized in the organic solvent (DMF) show excellent photocatalytic performance. We also used sodium oleate (SO) as the surfactant to assist the stabilization of RGOs in aqueous solutions and facilitate the fabrication of Ag_3PO_4 and RGOs. However, the as-prepared $\text{Ag}_3\text{PO}_4/\text{RGOs-SO}$ nanocomposites exhibit lower photocatalytic activity than pure Ag_3PO_4 (Fig. S7). The poor photocatalytic activity of $\text{Ag}_3\text{PO}_4/\text{RGOs-SO}$ composites could be resulting from the residual surfactant that was not removed completely by centrifuge washing. The preparation details and results are shown in *Supplementary data*.

To compare the photocatalytic stability of the pure Ag_3PO_4 nanoparticles and $\text{Ag}_3\text{PO}_4/\text{RGOs}$ nanocomposite synthesized in DMF solvent, the used pure Ag_3PO_4 nanoparticles and $\text{Ag}_3\text{PO}_4/\text{RGOs}$ nanocomposite were collected and reused in three successive MB degradation experiments, respectively. As shown in Fig. 9a, the photocatalytic activity of $\text{Ag}_3\text{PO}_4/\text{RGOs}$

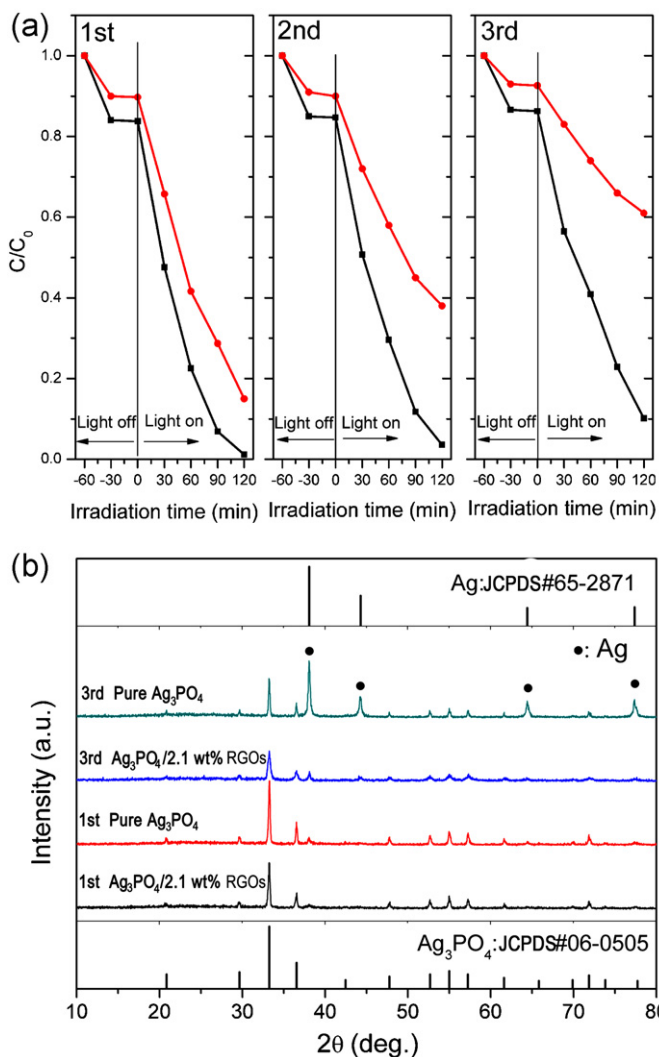


Fig. 9. (a) Repeated photocatalytic degradation of MB solution under visible light irradiation (square: $\text{Ag}_3\text{PO}_4/2.1\text{ wt\% RGOs}$ nanocomposite; circle: pure Ag_3PO_4 nanoparticles); (b) XRD patterns of $\text{Ag}_3\text{PO}_4/2.1\text{ wt\% RGOs}$ nanocomposite and pure Ag_3PO_4 nanoparticles after the first and third cycle experiments.

nanocomposite is decreased slowly in three successive experimental runs. However, the rate of MB degradation for pure Ag_3PO_4 nanoparticles decreases more significantly in three successive experimental runs under the same conditions. This result indicates that the $\text{Ag}_3\text{PO}_4/\text{RGOs}$ nanocomposite is more stable than the pure Ag_3PO_4 nanoparticles.

To evaluate the structural stability, the crystalline structures of pure Ag_3PO_4 and $\text{Ag}_3\text{PO}_4/\text{RGOs}$ nanocomposite after the first and third cycle experiments were studied (as shown in Fig. 9b). It can be seen that a small diffraction peak of metallic silver (Ag) appeared in the XRD pattern of pure Ag_3PO_4 after the first cycle experiment, indicating that the reduction of Ag_3PO_4 into metallic Ag particles had taken place during the MB degradation process. However, no evident crystalline structure changes could be observed in the XRD pattern of $\text{Ag}_3\text{PO}_4/\text{RGOs}$ nanocomposite after the first cycle experiment, indicating that RGOs improved the stability of the Ag_3PO_4 photocatalyst. After three successive experimental runs, obvious diffraction peaks of metallic Ag appeared in the XRD pattern of pure Ag_3PO_4 , indicating that Ag_3PO_4 was partially reduced into metallic Ag particles during the photocatalytic degradation process. When $\text{Ag}_3\text{PO}_4/\text{RGOs}$ nanocomposite was used as the photocatalyst to carry out the repeated photocatalytic degradation experiment,

there are small diffraction peaks of metallic Ag appeared in the XRD pattern after three successive experimental runs. The phase content of a sample can be calculated from the integrated intensities of diffraction peaks from the XRD pattern [63,64]. The weight fraction of metallic Ag (W_A) can be calculated from the equation below:

$$W_A = \frac{I_A}{I_A + (I_B/K_A^B)} \quad (3)$$

where I_A and I_B represent the integrated intensity of the Ag peaks and Ag_3PO_4 peaks, respectively. K_A^B represents the specific value of reference intensity ratio (RIR) of Ag_3PO_4 and Ag, which is determined to be 2.66.

The calculated weight fraction of metallic Ag (W_A) for $\text{Ag}_3\text{PO}_4/\text{RGOs}$ nanocomposite after three successive experimental runs is 35.9%, which is lower than that of pure Ag_3PO_4 (81.4%). This result clearly indicates that the structural stability of Ag_3PO_4 is improved with the addition of RGOs, because RGOs might be used as protective coatings that inhibit the photocorrosion of Ag_3PO_4 .

4. Conclusions

The $\text{Ag}_3\text{PO}_4/\text{RGOs}$ nanocomposites have been successfully and directly produced *via* a facile chemical precipitation approach in DMF solvent without any hard/soft templates. Due to the photo-generated electron gathered on RGOs, $\text{Ag}_3\text{PO}_4/\text{RGOs}$ nanocomposites prefer to adsorb positively charged MB molecules rather than negatively charged MO molecules. Among a series of $\text{Ag}_3\text{PO}_4/\text{RGOs}$ nanocomposites, the $\text{Ag}_3\text{PO}_4/2.1\text{ wt\% RGOs}$ nanocomposite shows the best photocatalytic activity despite degradation of MB or MO. In addition to the significant improvement in photocatalytic activity, the $\text{Ag}_3\text{PO}_4/\text{RGOs}$ nanocomposites are more stable than pure Ag_3PO_4 since the RGOs can be used as protective coatings that partially inhibit the photocorrosion of Ag_3PO_4 . The $\text{Ag}_3\text{PO}_4/\text{RGOs}$ nanocomposites with excellent photocatalytic performance and enhanced stability could find promising applications in addressing environmental protection issues. In summary, this work not only promotes the development of Ag_3PO_4 for practical applications, but also inspires the exploration of similar facile methods to stabilize other easily photocorroded photocatalysts.

Acknowledgements

This work is financially supported by National Science Foundation for Distinguished Young Scholars (No. 50925206). We wish to thank Dr. Xianzhi Wang (College of Pastoral Agriculture Science and Technology, Lanzhou University) for the TOC measurements.

Appendix A. Supplementary data

Supplementary data associated with this article can be found, in the online version, at <http://dx.doi.org/10.1016/j.apcatb.2012.11.022>.

References

- [1] S. Anandan, A. Vinu, T. Mori, N. Gokulkrishnan, P. Srinivasu, V. Murugesan, K. Ariga, *Catal. Commun.* 8 (2007) 1377–1382.
- [2] Y. Liu, L. Fang, H. Lu, L. Liu, H. Wang, C. Hu, *Catal. Commun.* 17 (2011) 200–204.
- [3] Z. Yi, J. Ye, N. Kikugawa, T. Kako, S. Ouyang, H. Stuart-Williams, H. Yang, J. Cao, W. Luo, Z. Li, *Nat. Mater.* 9 (2010) 559–564.
- [4] Y. Bi, S. Ouyang, N. Umezawa, J. Cao, J. Ye, *J. Am. Chem. Soc.* 133 (2011) 6490–6492.
- [5] Y. Bi, H. Hu, S. Ouyang, G. Lu, J. Cao, J. Ye, *Chem. Commun.* 48 (2012) 3748–3750.
- [6] C.T. Dinh, T.D. Nguyen, F. Kleitz, T.O. Do, *Chem. Commun.* 47 (2011) 7797–7799.
- [7] H. Wang, Y. Bai, J. Yang, X. Lang, J. Li, L. Guo, *Chem. Eur. J.* 18 (2012) 5524–5529.
- [8] Y. Bi, S. Ouyang, J. Cao, J. Ye, *Phys. Chem. Chem. Phys.* 13 (2011) 10071–10075.
- [9] S.B. Rawal, S.D. Sung, W.I. Lee, *Catal. Commun.* 17 (2011) 131–135.
- [10] W. Yao, B. Zhang, C. Huang, C. Ma, X. Song, Q. Xu, *J. Mater. Chem.* 22 (2012) 4050–4055.

[11] Y. Liu, L. Fang, H. Lu, Y. Li, C. Hu, H. Yu, *Appl. Catal. B* 115–116 (2012) 245–252.

[12] L. Zhang, H. Zhang, H. Huang, *New J. Chem.* 36 (2012) 1541–1544.

[13] G. Li, L. Mao, *RSC Adv.* 2 (2012) 5108–5111.

[14] H. Zhang, H. Huang, H. Ming, L. Zhang, *J. Mater. Chem.* 22 (2012) 10501–10506.

[15] M. Ishigami, J. Chen, W. Cullen, M. Fuhrer, E. Williams, *Nano Lett.* 7 (2007) 1643–1648.

[16] H.-K. Kim, S.-M. Bak, K.-B. Kim, *Electrochem. Commun.* 12 (2010) 1768–1771.

[17] A.K. Geim, K.S. Novoselov, *Nat. Mater.* 6 (2007) 183–191.

[18] H.K. Chae, D.Y. Siberio-Pérez, J. Kim, Y.B. Go, M. Eddaoudi, A.J. Matzger, M. O'Keeffe, O.M. Yaghi, *Nature* 427 (2004) 523–527.

[19] K.P. Loh, Q. Bao, P.K. Ang, J. Yang, *J. Mater. Chem.* 20 (2010) 2277–2289.

[20] E. Belyarova, M.E. Itkis, P. Ramesh, C. Berger, M. Sprinkle, W.A. de Heer, R.C. Haddon, *J. Am. Chem. Soc.* 131 (2009) 1336–1337.

[21] G. Williams, B. Seger, P.V. Kamat, *ACS Nano* 2 (2008) 1487–1491.

[22] H. Zhang, X. Lv, Y. Li, Y. Wang, J. Li, *ACS Nano* 4 (2010) 380–386.

[23] H.J. Shin, K.K. Kim, A. Benayad, S.M. Yoon, H.K. Park, I.S. Jung, M.H. Jin, H.K. Jeong, J.M. Kim, J.Y. Choi, *Adv. Funct. Mater.* 19 (2009) 1987–1992.

[24] S. Yin, Y. Aita, M. Komatsu, J. Wang, Q. Tang, T. Sato, *J. Mater. Chem.* 15 (2005) 674–682.

[25] S. Stankovich, D.A. Dikin, R.D. Pineri, K.A. Kohlhaas, A. Kleinhammes, Y. Jia, Y. Wu, S.B.T. Nguyen, R.S. Ruoff, *Carbon* 45 (2007) 1558–1565.

[26] S. Park, R.S. Ruoff, *Nat Nano* 4 (2009) 217–224.

[27] D. Li, M.B. Muller, S. Gilje, R.B. Kaner, G.G. Wallace, *Nat. Nanotechnol.* 3 (2008) 101–105.

[28] S. Villar-Rodil, J.I. Paredes, A. Martinez-Alonso, J.M.D. Tascon, *J. Mater. Chem.* 19 (2009) 3591–3593.

[29] H. Wang, J.T. Robinson, X. Li, H. Dai, *J. Am. Chem. Soc.* 131 (2009) 9910–9911.

[30] V. Romanov, C.-K. Siu, U.H. Verkerk, A.C. Hopkinson, K.W.M. Siu, *J. Phys. Chem. A* 114 (2010) 6964–6971.

[31] G.R. Bamwenda, H. Arakawa, *Appl. Catal. A* 210 (2001) 181–191.

[32] H. Li, J. Li, Y. Huo, *J. Phys. Chem. B* 110 (2006) 1559–1565.

[33] G. Jiang, Z. Lin, C. Chen, L. Zhu, Q. Chang, N. Wang, W. Wei, H. Tang, *Carbon* 49 (2011) 2693–2701.

[34] C. Nethravathi, M. Rajamathi, *Carbon* 46 (2008) 1994–1998.

[35] A.V. Murugan, T. Murali, A. Manthiram, *Chem. Mater.* 21 (2009) 5004–5006.

[36] L.M. Miller, V. Vairavamurthy, M.R. Chance, R. Mendelsohn, E.P. Paschal, F. Betts, A.L. Boskey, *Biochim. Biophys. Acta* 1527 (2001) 11–19.

[37] S. Gadaleta, E. Paschal, F. Betts, R. Mendelsohn, A. Boskey, *Calcif. Tissue. Int.* 58 (1996) 9–16.

[38] Z. Li, J. Wang, S. Liu, X. Liu, S. Yang, *J. Power Sources* 196 (2011) 8160–8165.

[39] R.L. Frost, A.W. Musumeci, J.T. Kloprogge, M.O. Adebajo, W.N. Martens, *J. Raman Spectrosc.* 37 (2006) 733–741.

[40] M. Lopez-Bote, S. Montero, *J. Raman Spectrosc.* 9 (1980) 386–392.

[41] Y. Wang, R. Shi, J. Lin, Y. Zhu, *Appl. Catal. B* 100 (2010) 179–183.

[42] Y. Zhang, Z.-R. Tang, X. Fu, Y.-J. Xu, *ACS Nano* 4 (2010) 7303–7314.

[43] P. Dong, Y. Wang, L. Guo, B. Liu, S. Xin, J. Zhang, Y. Shi, W. Zeng, S. Yin, *Nanoscale* 4 (2012) 4641–4649.

[44] H. Tong, S. Ouyang, Y. Bi, N. Umezawa, M. Oshikiri, J. Ye, *Adv. Mater.* 24 (2012) 229–251.

[45] R. Czerw, B. Foley, D. Tekleab, A. Rubio, P.M. Ajayan, D.L. Carroll, *Phys. Rev. B* 66 (2002) 033408.

[46] Z. Xiong, L.L. Zhang, J. Ma, X.S. Zhao, *Chem. Commun.* 46 (2010) 6099–6101.

[47] Y. Xu, M.A.A. Schoonen, *Am. Mineral.* 85 (2000) 543–556.

[48] Y. Ocak, M. Kulakci, T. Kılıçoğlu, R. Turan, K. Akkılıç, *Synth. Met.* 159 (2009) 1603–1607.

[49] J.S. Lee, K.H. You, C.B. Park, *Adv. Mater.* 24 (2012) 1084–1088.

[50] L. Zang, C.Y. Liu, X.M. Ren, *J. Photochem. Photobiol. A* 85 (1995) 239–245.

[51] T. Florence, *Aust. J. Chem.* 18 (1965) 609–618.

[52] J. Zhang, Z. Xiong, X.S. Zhao, *J. Mater. Chem.* 21 (2011) 3634–3640.

[53] L. Ge, *J. Mol. Catal. A: Chem.* 282 (2008) 62–66.

[54] D. Yang, H. Liu, Z. Zheng, Y. Yuan, J.-c. Zhao, E.R. Waclawik, X. Ke, H. Zhu, *J. Am. Chem. Soc.* 131 (2009) 17885–17893.

[55] B. Li, H. Cao, *J. Mater. Chem.* 21 (2011) 3346–3349.

[56] J.G. Yu, T.T. Ma, S.W. Liu, *Phys. Chem. Chem. Phys.* 13 (2011) 3491–3501.

[57] Q. Li, B. Guo, J. Yu, J. Ran, B. Zhang, H.-J. Yan, J.R. Gong, *J. Am. Chem. Soc.* 133 (2011) 10878–10884.

[58] B. Liu, Y. Huang, Y. Wen, L. Du, W. Zeng, Y. Shi, F. Zhang, G. Zhu, X. Xu, Y. Wang, *J. Mater. Chem.* 22 (2012) 7484–7491.

[59] Y. Shiraishi, N. Saito, T. Hirai, *J. Am. Chem. Soc.* 127 (2005) 12820–12822.

[60] Q. Xiang, J. Yu, M. Jaroniec, *Chem. Commun.* 47 (2011) 4532–4534.

[61] Y. Akama, A. Tong, M. Ito, S. Tanaka, *Talanta* 48 (1999) 1133–1137.

[62] L. Gomathi Devi, B. Narasimha Murthy, S. Girish Kumar, *Chemosphere* 76 (2009) 1163–1166.

[63] H. Zhang, J.F. Banfield, *J. Phys. Chem. B* 104 (2000) 3481–3487.

[64] A.A. Gribb, J.F. Banfield, *Am. Mineral.* 82 (1997) 717–728.